PHYSICAL REVIEW D **90,** 023014 (2014)

Wavefront twisting by rotating black holes: Orbital angular momentum generation and phase coherent detection

Huan Yang[1,2,*] and Marc Casals[3,†]

[1]*Perimeter Institue for Theoretical Physics, Waterloo, Ontario N2L2Y5, Canada*
[2]*Institute for Quantum Computing, University of Waterloo, Waterloo, Ontario N2L3G1, Canada*
[3]*Institute of Cosmology, Relativity and Astrophysics, Centro Brasileiro de Pesquisas Físicas, Rio de Janeiro CEP 22290-180, Brazil*

(Received 12 April 2014; published 17 July 2014)

In this paper we study wave propagation and scattering near a black hole. In particular, we assume a coherent emission source near the black hole and investigate the wavefront distortion as seen by a distant observer. By ignoring the spin nature of the electromagnetic radiation we model it by a complex scalar field. Then, the propagating wave near the observer can be decomposed using the Laguerre-Gaussian mode basis and its wavefront distortion can be characterized by the decomposition coefficient. We find that this decomposition spectrum is symmetric with respect to the azimuthal quantum number in the case that the wave source is located near a nonrotating (Schwarzschild) black hole, whereas the spectrum is generically asymmetric if the host black hole is rotating (Kerr). The spectral asymmetry, or the net orbital angular momentum carried by the wave, is intimately related to the black-hole spin and mass, the wave frequency and the locations of the source and the observer. We present semianalytical expressions and numerical results for these parameter dependences. If the emitted radiation is temporally coherent, our results show that the secondary images (arising from the orbiting of the wavefront around the black hole) of the source can be almost as bright as its primary image. Separately, in the case of temporally incoherent radiation, we show that the nonfundamental spectrum components in the primary image could be resolved by spatially separated telescopes, although that would be degenerate with the telescope direction. Finally, our results suggest that the black-hole-induced spectral asymmetry is generally too weak to be observed in radio astronomy, even if the observer is located near an optical caustic.

DOI: 10.1103/PhysRevD.90.023014 PACS numbers: 95.85.Bh, 04.25.-g, 04.30.Db, 04.70.Bw

I. INTRODUCTION

Photon orbital angular momentum (POAM), as compared to photon spin angular momentum, was less known in optics up until about two decades ago, mostly due to the technical difficulties in generating light with definite POAM states and in finding appropriate applications for such light. In 1990, Tamm and Weiss [1] first managed to produce Laguerre-Gaussian (LG) laser beams in the laboratory, which have helical phase front and quantized POAM.[1] Their studies paved the way for later proposals on applications of LG modes, including applications on quantum information processing and quantum cryptography [2–5], or even on future generations of gravitational wave detectors [6].

In addition, Harwitt [7] proposed several astrophysical sources or mechanisms that possibly introduce nonzero POAM to light. These sources and mechanisms include maser beams that pass through inhomogeneous interstellar medium, luminous pulsars or quasars, and waves passing through the vicinity of a rotating black hole. Recently, Tamburini *et al.* [8] performed a numerical simulation of radio emissions from an accretion disk surrounding a rotating black hole, assuming that different radiative sources in the disk are spatially coherent. In the simulation, they observed nontrivial POAM generation and asymmetric spectra in terms of the LG-mode basis depending on the spin of the host black hole and the observer's location in the sky. It remains physically important to understand the physical mechanism for the generation of light with POAM near black holes, and obtain estimates for the POAM magnitude, which apparently encodes information about the host black hole.

In this study we analyze the scalar wave emission from a coherent point source near a Kerr or a Schwarzschild black hole. We note that although the case of the electromagnetic wave which is considered in the above studies is a spin-1 field, in this paper we consider instead a complex scalar field, which has zero spin. We use the scalar field as a model for the electromagnetic field when its spin character is neglected. We employ this scalar model since it is a technically simpler case to study than the electromagnetic case and yet it is sufficient in order to understand the generation of POAM spectra. By assuming the wavelength of the radiation (not greater than mm scale) to be much smaller than the size of the black hole (not less than km

*hyang@perimeterinstitute.ca
†mcasals@cbpf.br

[1]LG modes are spatial eigenmodes of a wave which is freely propagating under the paraxial approximation and which has integer orbital angular momentum. See Sec. II for further details.

scale), we calculate the wave received by a distant observer on the celestial sphere and the corresponding POAM spectrum. We investigate both cases where the emission is temporally coherent and incoherent, as the two cases produce different POAM spectra. For completeness, we also study the scenario where the observer is located near an optical caustic of the background space-time, in which case the POAM asymmetry could be amplified, in addition to the wave itself.

Part of the wave emitted from the vicinity of the black hole immediately propagates outwards and reaches the faraway observer, thus yielding the so-called primary image. However, other parts of the wave will typically orbit around the black hole a number of times before leaving the vicinity of the black hole and propagating outwards to reach the faraway observer; these wave signals will correspond to secondary images. We obtain the propagation of the wave via the calculation of an approximation to the retarded Green function of the wave equation in Kerr space-time. For the primary image we approximate the Green function by using the so-called Hadamard form (see, e.g., [9]) and a calculation of the so-called van Vleck determinant, a biscalar which measures the degree of focusing of neighboring null geodesics. As for the later images—for which the Hadamard form is not valid—we instead approximate the Green function by a calculation of the quasinormal modes in Kerr space-time in the high-oscillation-frequency limit (see, e.g., [10]).

We shall show that, although the emission from a single nonrotating star in flat space-time generally contains only the fundamental LG mode (which contains zero angular momentum) at far distances, the presence of a rotating black hole near the star will generate a nontrivial POAM spectrum. Such spectrum is symmetric with respect to the LG basis (i.e., with respect to the azimuthal quantum number) for nonrotating Schwarzschild black holes and generically asymmetric for rotating Kerr black holes. That is, the asymmetric part of the spectrum contains the spin information of rotating black holes. As we shall show in Sec. II C, the symmetric part of a POAM spectrum may be affected by the direction of the observation plane of a telescope array. This further emphasizes the importance of measuring the asymmetric part of the spectrum.

An important difference between the case we study in this paper and that in [8] is that here, as opposed to [8], we have a pointlike emission source. Therefore, the interference between waves emitted from sources at different spatial locations that occurs in [8] is absent here. In our case, the main effect comes only from gravitationally twisting/merging the light bundles from a single emission source and we therefore expect the spectral asymmetry to be much smaller than in [8] (see Secs. IV and V for details).

This paper is organized as follows. In Sec. II we review the decomposition of a paraxial wave with respect to the LG basis, the definition of a POAM spectrum and the related quantity for detection. In Sec. III we describe the methods used for the calculation of the Green function. In Sec. IV we analyze the wave emitted by a source near a black hole, using the Green function approach, and present our POAM results. In Sec. V we investigate the setting where the observer is located near an optical caustic and we conclude in Sec. VI. Throughout this paper, we use geometric units $G = c = 1$, the black-hole mass M is also set to 1, unless otherwise specified, and the metric signature is taken to be $(-+++)$.

II. OVERVIEW OF POAM AND SPECTRAL DECOMPOSITION

In this section, we present a cursory review of the LG modes of light and the corresponding POAM-spectrum decomposition, which is useful for later sections. Interested readers may find a detailed discussion in [11] on topics such as POAM observables in astronomy, the propagation or map of POAM from the celestial sphere onto detectors, the detection of POAM using existing astronomical instruments, etc.

A. Mode decomposition

Let us consider a light beam propagating on a general space-time. We now describe two approximations. We will apply the first to the propagation of the beam all the way from the source to the observer (i.e., throughout the curved space-time), while will apply the second one only near the observer (i.e., where the space-time is asymptotically flat).

The first approximation is the "scalar field approximation," under which the vector character of the electromagnetic field is neglected. Under this approximation, the electromagnetic field is just described by a distribution of the field amplitude and phase, which is given by a complex scalar wave function $\Psi(x)$ that satisfies the Klein-Gordon equation:

$$\Box\Psi(x) = \frac{1}{\sqrt{-g}}\partial_\mu(\sqrt{-g}g^{\mu\nu}\partial_\nu\Psi(x)) = -4\pi\mu(x), \tag{2.1}$$

where x is a space-time point, $g_{\mu\nu}$ is the background space-time metric, $g(x) \equiv \det(g_{\mu\nu}(x))$ and $\mu(x)$ is the source of the field. Physically, this approximation is valid, for example, when one of the components of the traverse field dominates over the other one. In flat space-time (such as near the observation plane in an astrophysical context), where it is a common approximation (e.g., [11,12]), one may alternatively view the scalar field Ψ as representing one of the Cartesian components of the electric or magnetic field. In curved space-time, we expect this approximation to be valid in the high-frequency limit that we adopt in this paper, particularly in the situation of Sec. IV B where only

the part of the wave on, or closely near, one single image (the primary one) is considered. In the situation of Sec. IV A, where various images—which follow different paths around the black hole—are considered this approximation may be less valid, because the polarization of the electromagnetic field could rotate differently along different path. In that case, more careful analysis has to be done to take into account the rotation of field polarizations.

Let us now carry out a Fourier-mode decomposition of the complex scalar field $\Psi(x)$ and denote its Fourier modes by $\psi_\omega = \psi_\omega(\mathbf{x})$, where $\mathbf{x}$ denotes the spatial coordinates of x and ω the frequency. Since in this paper we will be considering a source radiating with a single frequency, the spatial part of the total field $\Psi(x)$ will be given by a single Fourier mode [see Eq. (3.6) below; the only exception will be in Eq. (4.9)].

In order to introduce the LG mode decomposition now and for the rest of this subsection we assume flat space-time. Even though in this paper we deal with the presence of a black hole, the emitted wave will propagate from the strong field near the black hole all the way to Earth, where the space-time is asymptotically flat. Here, a connection can be made between the emitted wave as detected on Earth and the LG basis defined in flat space-time. In flat space-time, the Fourier modes satisfy the Helmholtz equation:

$$(\nabla^2 + \omega^2)\psi_\omega = 0, \tag{2.2}$$

where $\omega = ||\vec{k}||$, $\vec{k}$ is the wave vector and ∇^2 is the Laplacian operator in flat space-time.

The LG basis requires a second approximation: the paraxial approximation, under which the wave propagates approximately along an axis, say the Z axis (i.e., k_X, $k_Y \ll k_Z \approx ||\vec{k}||$ using Cartesian coordinates). This is generally a good approximation when the light (even though strictly speaking we are now dealing with a scalar field, we use it to model light—within the scalar field approximation—and so at times we might still refer to the wave as "light") is far away from its emission source. This approximation is well justified in the astrophysical setting when the wave has reached a distant observer after traveling all the way from near the black hole and so the celestial sphere is locally a plane. Under the paraxial approximation the spatial wave function ψ_ω can be expanded as a family of LG modes u_{pl}, which have the following form (e.g., [13]):

$$u_{pl}(Z,\rho,\varphi) = \frac{C}{w(Z)}\left(\frac{\rho\sqrt{2}}{w(Z)}\right)^{|l|} e^{-\rho^2/w(Z)^2} L_p^{|l|}\left(\frac{2\rho^2}{w(Z)^2}\right) e^{i\omega\rho^2/(2R(Z))} e^{il\varphi} e^{i(2p+|l|+1)\xi(Z)+i\omega Z}, \tag{2.3}$$

where we use a cylindrical coordinate system (Z,ρ,φ) for the spatial point $\mathbf{x}$, C is a normalization constant, $L_p^{|l|}$ is a Laguerre polynomial, l is the azimuthal quantum number and p is the radial quantum number. We have defined the functions

$$\begin{aligned} w(Z) &\equiv w_0\sqrt{1 + Z^2/z_R^2}, \\ R(Z) &\equiv Z\left(1 + \frac{Z_R^2}{Z^2}\right), \\ \xi(Z) &\equiv \arctan(Z/Z_R), \end{aligned} \tag{2.4}$$

where w_0 is the size of the beam waist, $Z_R \equiv \pi w_0^2/\lambda$ is the Rayleigh length and $\lambda = 2\pi/k$ is the wavelength of the light.

Because of the $e^{il\varphi}$ factor, the phase fronts of LG modes (except for the fundamental mode $l = 0$) are helical, and the mode with indices $\{l, p\}$ carries a definite orbital angular momentum $l\hbar$ per photon. This can be intuitively understood by noticing that the wave vectors are spiraling around the propagation (Z) axis (k_X and k_Y are small but nonzero). It can also be shown that LG modes form a complete basis for all the paraxial waves with the same frequency. Therefore, at a given value of Z, any spatial wave function ψ_ω can be decomposed in the basis of LG modes as

$$\psi_\omega(Z,\rho,\varphi) = \sum_{p=0}^{\infty}\sum_{l=-\infty}^{\infty} c_{pl}(Z) u_{pl}(Z,\rho,\varphi), \tag{2.5}$$

where the coefficients are given by

$$c_{pl}(Z) = \langle u_{pl}|\psi_\omega\rangle, \tag{2.6}$$

where the product of any two spatial functions u and ψ_ω is defined on the constant-Z plane as

$$\langle u|\psi_\omega\rangle \equiv \int_0^{2\pi} d\varphi \int_0^{\infty} d\rho\rho u^*(Z,\rho,\varphi)\psi_\omega(Z,\rho,\varphi). \tag{2.7}$$

For the purpose of understanding the generation of POAM spectra, there is limited interest in distinguishing the radial profile of the wave function. As a result, we sum up all the radial components for each value of l, so that the decomposition becomes

$$\psi_\omega(Z,\rho,\varphi) = \sum_{l=-\infty}^{\infty} e^{il\varphi}\psi_{\omega,l}(Z,\rho), \tag{2.8}$$

where $\psi_{\omega,l}$ is given by

$$\psi_{\omega,l}(Z,\rho) = \frac{1}{2\pi}\int_0^{2\pi} d\varphi e^{-il\varphi}\psi_\omega(Z,\rho,\varphi). \tag{2.9}$$

We further define the spectra weight w_l of the POAM decomposition as

$$w_l = \frac{2\pi}{I}\int_0^\infty d\rho\rho|\psi_{\omega,l}|^2, \tag{2.10}$$

$$I \equiv \int_0^\infty d\rho \int_0^{2\pi} \rho d\varphi|\psi_\omega|^2. \tag{2.11}$$

Based on their definition, it is easy to verify that the weights w_l satisfy the normalization condition $\sum_l w_l = 1$, and so the averaged POAM per photon is given by

$$\bar{L}_Z = \hbar\sum_{l=-\infty}^{\infty} l w_l. \tag{2.12}$$

The definition of w_l can easily be generalized [11] to incoherent light by decomposing the wave function as a summation of coherent pieces and dropping the mutual-interference terms. Its physical properties can be further elaborated by studying the two following simple examples.

B. Examples

In the first example, we note that a plane wave, with its propagation direction orthogonal to the observation plane, satisfies $w_l = \delta_{l0}$, i.e., all modes have zero spectra weight except for the fundamental mode. This fact is important as any initially distorted wavefront always tends to flatten out during propagation in free space, because of the diffraction effect. Since real telescopes have a finite collection area, which also means that the integration upper bound for ρ in Eqs. (2.10) and (2.11) should be replaced by the instrument's size, the spectra weights for the modes with $|l| > 0$ always decrease as we increase the distance between the detector and the source.

In the second example, if the wave function has a dependence $\psi_\omega = e^{i\Phi(Z,\rho,\varphi)}$, where $\Phi(Z,\rho,\varphi)$ is a real-valued function, it can be shown that the w_l's are generically nonzero and the spectrum must be symmetric, i.e., $w_l = w_{-l}$ (see Sec. IV B for a proof in the case $l = \pm 1$; the generalization to higher $|l|$ is trivial). In fact, if we draw the normal vectors to the constant-phase plane of a LG mode with $l \neq 0$, it shows a spiraling pattern which geometrically resembles a twisted light bundle. This twisting of light can be generated, for example, by the frame dragging caused by a rotating black hole (Sec. IV B), by merging adjacent light bundles near an optical caustic (Sec. V), or even by the offset interference between previously far-apart geometric rays (Sec. IV A)—see Fig. 1. In all these scenarios, we observe variations in both the phase and the amplitude. This is also true for the LG modes as shown in Eq. (2.3), where we find zero intensity at the origin ($\rho = 0$) and nonzero amplitude elsewhere.

When dealing with actual observables, it is more convenient to use $\sqrt{w_l}$ rather than w_l, because $\sqrt{w_l}$ is directly proportional to the wave amplitude at each l, which is an observable obtainable by Eq. (2.9) or physically using an antenna array as illustrated in [14]. As a consequence,

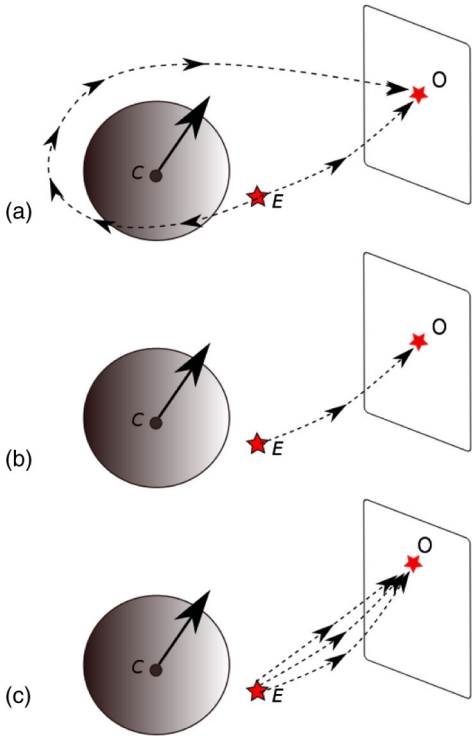

FIG. 1 (color online). An illustration of the three scenarios discussed in Secs. IV A, IV B and V respectively. (a) The interference between two distinct rays that emit from E and meet each other at the observer O. (b) No interference between different rays. The light bundle of the primary ray is slightly twisted by the rotating black-hole space-time. (c) Interference between adjacent light bundles. This only happens when the observer O is located near an optical caustic of the emission from E.

although we shall refer to $|\sqrt{w_l} - \sqrt{w_{-l}}|$ as the spectral asymmetry throughout this paper, more strictly speaking it corresponds to the "amplitude" asymmetry. This amplitude asymmetry can be measured by comparing phases on different sites of the telescope array, and its detectability is closely related to the phase sensitivity of the telescope array. The ground-based radio telescopes suffer from air-turbulence-induced phase errors, and by implementing novel techniques, such as measuring the *closure phase* [15], the phase sensitivity can be improved to a scale of multiple wavelengths [16].

C. Spectral degeneracy

A symmetric weight spectrum can be generated by tilting the observation plane with respect to the optical axis, as this generally introduces an $e^{i\omega r_f(\alpha x_1+\beta x_2)}$ factor into the wave, depending on the tilt angles α and β, where r_f is the radius between the source (or approximately the black hole) and the observation plane, and $x_{1,2}$ are coordinates on the observation plane defined in Sec. IV A. Even for an incoming plane wave, this phase factor will generate a *symmetric* POAM spectrum, with $w_1 = w_{-1} \propto \omega^2 b^2(\alpha^2 + \beta^2)$, where b is the

size of the detector. Unless the tilt angles are known within an accuracy of M/r_f, which is an unrealistic requirement, it generates a much larger symmetric POAM spectrum than the $l \neq 0$ components of the POAM spectrum induced by a rotating black-hole geometry. Thus, the physics carried by a symmetric POAM is degenerate with the tilt angle of the observation plane, and is not likely to be decoded via radio observations alone.

III. GREEN FUNCTION METHOD

In order to determine the wave emission by a point source, we shall make use of the retarded Green function of the wave equation (2.1) satisfied by the field propagating in the background space-time. The retarded Green function can also be used to calculate the self-force on a small compact object moving on the background of a massive black hole (see, e.g., [9]) and the associated radiation backreaction. Techniques for the calculation of the Green function for field perturbations of different spin in Schwarzschild, Kerr or other more exotic background space-times have been recently developed [10,17–21] and applied [22–24] with success to the calculation of the self-force. In this paper we will employ some of these techniques for the calculation of the Green function to calculate the propagation of a scalar wave in Kerr space-time and we refer the reader to this literature for further details on the techniques.

As explained in Sec. II A, we use a massless, complex scalar field $\Psi(x)$ to model the electromagnetic field when its spin character is neglected. This scalar field propagating on a curved space-time obeys the Klein-Gordon equation (2.1). The retarded Green function satisfies this equation with an invariant Dirac-delta distribution in the source

$$\Box G_{\rm ret}(x,x') = -4\pi \frac{\delta_4(x-x')}{\sqrt{-g(x)}}, \tag{3.1}$$

subject to causal boundary conditions: $G_{\rm ret}(x,x')$ is zero if x does not lie in the causal future of x'. The propagation of the massless scalar wave is determined by the retarded Green function via

$$\Psi(x) = \int d^4x'' \sqrt{-g(x'')}\mu(x'')G_{\rm ret}(x,x''). \tag{3.2}$$

From now on we will focus on the case that the background space-time is Kerr space-time. Let us assume that there is an emitter following a worldline given by $x'(\tau)$, where τ is the proper time of the emitter, which is located near a rotating Kerr black hole and is radiating scalar waves with frequency ω_0 with respect to its proper reference frame. Specifically, we take the source to be

$$\mu(x) = \int_{-\infty}^{\infty} d\tau \frac{\delta_4(x-x'(\tau))}{\sqrt{-g(x)}} e^{-i\omega_0\tau}. \tag{3.3}$$

From Eq. (3.2), the wave that an observer located at the space-time point x receives is simply given by

$$\Psi(x) = \int_{-\infty}^{\infty} d\tau e^{-i\omega_0\tau} G_{\rm ret}(x,x'(\tau)). \tag{3.4}$$

Although the integration upper bound is here taken to be ∞, the integration actually contains only the causal contributions because the retarded Green function is zero if x does not lie in the causal future of x'. For simplicity, we assume hereafter that the emitter stays at a fixed spatial location $\mathbf{x}'$ at all times. Despite the fact that this is not a very physical scenario, it does not harm the main physical results and it simplifies the calculations. We define the time-dilation factor N and the rescaled frequency ω to be

$$N \equiv \sqrt{-g_{tt}(\mathbf{x}')}, \qquad \omega \equiv N\omega_0. \tag{3.5}$$

We also note that the time-translational symmetry of Kerr space-time implies $G_{\rm ret}(x,x') = G_{\rm ret}(\mathbf{x},\mathbf{x}';t-t')$ (with a slight abuse of notation). Using the fact that the proper time of the static emitter satisfies $d\tau = Ndt'$ and plugging Eq. (3.5) into Eq. (3.4), we obtain

$$\begin{aligned}\Psi(x) &= e^{i\omega t}\psi_\omega(\mathbf{x}),\\ \psi(\mathbf{x}) &= \int_{-\infty}^{\infty} dt\prime N \times e^{-i\omega(t-t')} G_{\rm ret}(x,x')\\ &= N\, G^{\omega}_{\rm ret}(\mathbf{x},\mathbf{x}'),\end{aligned} \tag{3.6}$$

where $G^{\omega}_{\rm ret}$ are the Fourier modes of the retarded Green function.

In the following subsections we will describe two different techniques for calculating the Fourier modes $G^{\omega}_{\rm ret}$, one technique being valid for the calculation of the primary image and the other for the calculation of the later, secondary images. Even though we develop the techniques for general Fourier frequencies, at some point in the analysis we will carry out approximations corresponding to the high-frequency limit for the radiation (i.e., $\omega \gg 1/M$) which, as mentioned in the Introduction, is the physical limit of interest in this paper.

A. Primary image: Hadamard form

In a "sufficiently" small neighborhood called a normal neighborhood[2] of the point x' of emission of the primary pulse, the retarded Green function can be calculated via the Hadamard form [9,25],[3]

[2]A normal neighborhood of x' is a region containing x' such that every point x in this region is connected to x' by a unique geodesic in that region.

[3]In principle, it should also be possible to express the Green function in the normal neighborhood via the spectroscopic decomposition of Eq. (3.16). However, in practice the convergence of $G_{\rm QNM}$ and $G_{\rm BC}$ is usually poor at very early times [26], and it is preferable to use the Hadamard form instead.

$$G_{\rm ret}(x,x') = [U(x,x')\delta(\sigma(x,x')) + V(x,x')H(-\sigma(x,x'))]H_+(x,x'). \quad (3.7)$$

Here, $U(x,x')$ and $V(x,x')$ are both smooth biscalars, $H(x)$ is the Heaviside distribution and $H_+(x,x')$ equals 1 if x lies to the future of x' and equals 0 otherwise. Synge's world function $\sigma(x,x')$ is given by

$$\sigma(x,x') = \frac{1}{2}(\bar{\lambda}_f - \bar{\lambda}_i)\int_{\bar{\lambda}_i}^{\bar{\lambda}_f} d\bar{\lambda} g_{\mu\nu}(\bar{z}) t^\mu t^\nu, \quad (3.8)$$

where the integration is performed along the unique geodesic $\bar{z}(\bar{\lambda})$ connecting x' and x, with $\bar{\lambda}$ being an affine parameter and $\bar{z}(\bar{\lambda}_i) = x'$ and $\bar{z}(\bar{\lambda}_f) = x$. Based on its definition, it is immediate to find that σ is positive if the geodesic joining x and x' is spacelike, negative if it is timelike and zero if it is null. Consequently, the term "$U\delta(\sigma)H_+$" in Eq. (3.7) only has support along the "direct" null wavefront that propagates from x' to x and so we will refer to it as the "direct part." We will refer to the points where this direct part of the null wavefront has support as the (future) light cone. The direct part of the Hadamard form, therefore, describes the primary image of a source at $\mathbf{x}'$ that an observer at $\mathbf{x}$ will detect.

The Fourier modes $G^\omega_{\rm dir}$ of the direct part of the Hadamard form correspond to the leading order of the Fourier modes of the full Green function in the geometrical optics limit (or under the WKB approximation). Thus, according to [21] they are given by

$$G^\omega_{\rm dir}(\mathbf{x},\mathbf{x}') = A_0(\mathbf{x},\mathbf{x}')e^{i\omega T_0(\mathbf{x},\mathbf{x}')}, \quad (3.9)$$

where $\omega T_0(\mathbf{x},\mathbf{x}')$ is the geometric phase for the direct null geodesic connecting x and x'. The amplitude $A_0(\mathbf{x},\mathbf{x}')$ is discussed in [21] in the context of mapping the areas of light bundles in a general curved space-time. In the remaining of this subsection we focus on the calculation of $A_0(\mathbf{x},\mathbf{x}')$ and $T_0(\mathbf{x},\mathbf{x}')$ in Kerr space-time.

By taking the Fourier transform of the direct part in Eq. (3.7) and comparing it with Eq. (3.9), it is straightforward to find that

$$A_0(\mathbf{x},\mathbf{x}') = \frac{U(x',x)}{|\partial\sigma/\partial t|_{t=T_0}}, \quad (3.10)$$

and $\sigma = 0$ when $t - t' = T_0(\mathbf{x},\mathbf{x}')$. In order to evaluate $\partial\sigma/\partial t$, we use a family of timelike geodesics for a particle with rest mass $m \to 0$ to asymptote to the null geodesic. For timelike geodesics, we take the affine parameter $\bar{\lambda}$ to be the proper time $\bar{\tau}$ along the timelike geodesic connecting x' and x, with $\bar{z}(\bar{\tau}_i) = x'$ and $\bar{z}(\bar{\tau}_f) = x$. Therefore, for timelike geodesics it is $\sigma = -(\bar{\tau}_f - \bar{\tau}_i)^2/2$ and we have

$$\left.\frac{\partial\sigma}{\partial t}\right|_{t=T_0} = -\lim_{m\to 0}(\bar{\tau}_f - \bar{\tau}_i)\left.\frac{\partial\bar{\tau}}{\partial t}\right|_{t=T_0,\text{fixed }\mathbf{x}'} = -\lim_{m\to 0}(\bar{\tau}_f - \bar{\tau}_i)u_t = \lim_{m\to 0}(\bar{\tau}_f - \bar{\tau}_i)\frac{E}{m} = \bar{\lambda}_f - \bar{\lambda}_i. \quad (3.11)$$

Here, $u_t = \partial_t \cdot u = -E/m$, where u is the 4-velocity, and E is the energy of the massive particle. Geodesics for any massless particle can be obtained by integrating out the equations of motion, which are separable in Boyer-Lindquist coordinates $\{r,\theta,\phi,t\}$ in Kerr space-time and they are given by [27]

$$\frac{dt}{d\bar{\lambda}} = \frac{[-a(aE\sin^2\theta - L_z) + (r^2+a^2)\Delta^{-1}P]}{r^2 + a^2\cos^2\theta},$$
$$\frac{d\phi}{d\bar{\lambda}} = \frac{[-(aE - L_z/\sin^2\theta) + a\Delta^{-1}P]}{r^2 + a^2\cos^2\theta},$$
$$\frac{d\theta}{d\bar{\lambda}} = \frac{[Q - \cos^2\theta(-a^2E^2 + L_z^2/\sin^2\theta)]^{1/2}}{r^2 + a^2\cos^2\theta},$$
$$\frac{dr}{d\bar{\lambda}} = \frac{\{P^2 - \Delta[Q + (L_z - aE)^2]\}^{1/2}}{r^2 + a^2\cos^2\theta}. \quad (3.12)$$

Here, E is the energy of the massless particle, L_z is the angular momentum of the particle along the z axis (the symmetric axis of the black hole, not to be confused with the Z axis, which is the axis of propagation of the wave used in Sec. II; similarly, here ϕ is the azimuthal angle with respect to the symmetry axis of the black hole whereas φ used in Sec. II was the azimuthal angle with respect to the axis of propagation of the wave) and Q, which shows up in the expressions for $d\theta/d\bar{\lambda}$ and $dr/d\bar{\lambda}$, is Carter's constant of motion. The functions Δ and P are given by

$$\Delta \equiv r^2 - 2Mr + a^2, \qquad P \equiv E(r^2+a^2) - L_z a, \quad (3.13)$$

where M and a are, respectively, the mass and the angular momentum of the Kerr black hole. We integrate the set of coupled, first-order ordinary differential equations Eq. (3.12) in order to obtain $(\bar{\lambda}_f - \bar{\lambda}_i)$ (and therefore $\partial\sigma/\partial t|_{t=T_0}$) along the desired direct null geodesic $\bar{z}(\bar{\lambda})$. Further below [namely in order to calculate $\partial T_0/\partial\zeta|_{\mathbf{x}_0}$ in Eq. (4.5)], we will also need the values of $\partial T_0/\partial\theta_f$ and $\partial T_0/\partial\phi_f$, where $\theta_f \equiv \theta(\bar{\lambda}_f)$ and $\phi_f \equiv \phi(\bar{\lambda}_f)$. In order to calculate these partial derivatives, we give small variations to E and L_z and find how T_0, θ_f and ϕ_f vary and we then apply the chain rule. We note that these variations in θ_f and ϕ_f allow us to find (an approximation to) the Jacobian $\frac{\partial\{\theta_f,\phi_f\}}{\partial\{E,L_z\}}$, which allows us to calculate the values of E and L_z required in order for the final spatial point $\mathbf{x}$ to remain the same as we vary the black-hole angular momentum a.

As for the bitensor $U(x,x')$, in four-dimensional space-times it is related to the van Vleck determinant $\Delta_{\bar{z}}(x,x')$ as $U(x,x') = \Delta_{\bar{z}}^{1/2}(x,x')$ and it obeys the following transport equation [9,17]:

$$\frac{d\Delta_{\bar{z}}^{1/2}}{d\bar{\lambda}} = \frac{(4-\sigma^{\alpha}{}_{\alpha})}{2\bar{\lambda}}\Delta_{\bar{z}}^{1/2}, \tag{3.14}$$

where $\sigma^{\alpha}{}_{\beta} \equiv \nabla_{\beta}\nabla^{\alpha}\sigma$. We obtain the van Vleck determinant along the null geodesic $\bar{z}(\bar{\lambda})$ connecting x' and x in Kerr space-time by solving a system of transport equations: Eq. (3.14) together with transport equations for $\sigma^{\alpha}{}_{\beta}$—we refer the reader to [17] for details. In principle, we expect the van Vleck determinant $\Delta_{\bar{z}}(x,x')$ to diverge when x and x' are connected by more than one null geodesic. In a spherically symmetric space-time such x' points correspond to points which lie along $\phi = 0$ or π, and $\Delta_{\bar{z}}(x,x')$ diverges there [17,22,28]; in Kerr space-time the distribution of such points is a lot richer—see Sec. V. In any case, we calculate $\Delta_{\bar{z}}(x,x')$ only along a direct null geodesic, which does not reintersect any other null geodesic that started off at the same initial space-time point x'. Therefore, we find that $U(x,x') = \Delta_{\bar{z}}^{1/2}(x,x')$ does not diverge anywhere where we need to evaluate it for the results in this paper.

Finally, the biscalar $V(x,x')$ may be expressed (in a normal neighborhood) in the following form (e.g., [18]):

$$V(x,x') = \sum_{k=0}^{\infty} v_k(\mathbf{x},\mathbf{x}')(t-t'-T_0(\mathbf{x},\mathbf{x}'))^k, \tag{3.15}$$

where the coefficients v_k are regular biscalar functions. Under a Fourier transformation and after taking the high-frequency limit ($M\omega \gg 1$), any terms with $k > 0$ will yield contributions of order $O(1/(\omega M))$, and so the main effect of $V(x,x')$ under this limit is given by v_0.

B. Later images: Spectroscopy decomposition

After the primary signal arrives at the observer, subsequent signals will continue arriving due to the fact that part of the null wavefront emitted by the source orbits around the black hole an unlimited number of times. These subsequent signals, however, cannot be described by the Hadamard form Eq. (3.7) since they do not lie in a normal neighborhood of the emission point. The technique that we will use in order to calculate an approximation to the Green function for points corresponding to the subsequent images is a spectroscopy decomposition in the complex-frequency plane.

When deforming the Fourier integral in the complex-frequency plane, the retarded Green function for a field propagating on a black-hole background space-time (see, e.g., [23,29,30] in Schwarzschild and [10] in Kerr) can be decomposed into three parts:

$$G_{\rm ret} = G_{\rm HF} + G_{\rm QNM} + G_{\rm BC}. \tag{3.16}$$

The first part in Eq. (3.16), $G_{\rm HF}$, corresponds to an integral along a high-frequency arc. It is believed [23,30] to describe the direct pulse that travels near the future light cone and to vanish after a certain finite time corresponding to a point not lying beyond the boundary of the normal neighborhood. Since we will only use the spectral decomposition (3.16) for points lying outside the normal neighborhood, we can ignore the contribution $G_{\rm HF}$.

The second part in Eq. (3.16), $G_{\rm QNM}$, corresponds to a sum over the residues at the poles (the so-called quasinormal mode frequencies) of the Fourier modes of the Green function. This "quasinormal mode (QNM) part" is related to wave scattering in the strong-gravity region. In particular, QNMs in the limit of high-oscillation frequency (i.e., large real part of the QNM frequency or, equivalently, $L \equiv \ell + 1/2 \gg 1$, where ℓ is the index for the polar angle eigenvalue in Boyer-Lindquist coordinates) in Schwarzschild and Kerr space-times are intimately connected with null geodesics on the photon spheres (e.g., [31,32]), and there is a one-to-one mapping that relates conserved quantities of these null geodesics to the QNM's frequency, angular eigenvalue, azimuthal quantum number, etc. Furthermore, it has been shown [10,19,23] that the QNM part yields the singularity of the Green function $G_{\rm ret}(x,x')$ whenever the two space-time points x and x' are connected via a null geodesic. The null wavefront emitted at x' will wrap itself around the black hole an unlimited number of times. Each time that the wavefront orbits around the black hole one more time, a null geodesic which is part of the wavefront will travel outwards to reach the spatial point $\mathbf{x}$. At each instant of time when a null geodesic reaches $\mathbf{x}$ the retarded Green function $G_{\rm ret}(x,x')$ diverges. Following this correspondence, it is clear that it is the high-oscillation-frequency limit of QNMs that we need to evaluate in order to obtain the null wavefront for the secondary images (in fact, we expect the high-oscillation-frequency approximation for the QNM contribution to work better as the real radiation frequency ω becomes larger, which is the physical limit of interest in this paper). In Kerr space-time the "QNM contribution" is derived in [10] in the high-oscillation-frequency limit and it is expressed as an asymptotic expansion

$$G_{\rm QNM}(x,x') \sim \sum_{k=1}^{\infty} G_k(x,x'). \tag{3.17}$$

The time-domain functions $G_k(x,x')$ are given by

$$G_k = \begin{cases} (-1)^{k/2}\pi\chi_{\rm e}\delta[\pi k + g_{\rm e}(\mu_{\rm e})], & k \text{ even}, \\ (-1)^{(k+1)/2}\frac{\chi_{\rm o}H[-\pi k - g_{\rm e}(\mu_{\rm e})]}{-\pi(k+1)-g_{\rm o}(\mu_{\rm o})}, & k \text{ odd}, \end{cases} \tag{3.18}$$

where $\mu_{\rm e/o}$ characterize the "shape" of a geodesic connecting x and x', $g_{\rm e/o}$ are the phase functions and $\chi_{\rm e/o}$ are the

excitation amplitudes—they are all regular functions of x, x' and the parameters of the black hole (their physical meanings and detailed expressions are given in Sec. V of [10]). The asymptotic expansion of Eq. (3.17) is valid in the limit when the space-time points x and x' are joined by a null geodesic. Here, k is a positive integer index that labels the singularities of the Green function at different times as the wavefront orbits around the black hole. In Schwarzschild space-time, k is also a label for the number of times that the null geodesic joining x and x' has crossed a caustic and we expect this to still be true in Kerr space-time. We note that here and throughout this subsection by "caustic" we mean a space-time point (say, x) where two or more null geodesics that started off at the same space-time point (say, x') meet. This meaning is different from that generally used in optics, which we define in Sec. V and use in the rest of the paper, where the optical phase is required to be stationary. We shall therefore refer to the latter as an "optical caustic" to differentiate it from the caustic that we have just defined and that we use in this subsection.

By applying a Fourier transform to the time-domain functions G_k we find that the even-k modes scale as $O(1)$ in the frequency domain, whereas the odd-k modes scale as $O(1/(\omega M))$ for large-frequency ωM. As mentioned in the Introduction, we assume the wavelength of the radiation to be much smaller than the size of the black hole and, therefore, in this $\omega \gg 1/M$ limit we neglect the odd-k modes. The total contribution from the even-k modes in the frequency domain is just[4]

$$G^{\omega}_{\mathrm{QNM,e}} = \sum_{\text{even } k=2}^{\infty} (-1)^{k/2} \frac{\pi \chi_{\mathrm{e}}}{\Omega_R(\mu_{\mathrm{e}})} e^{i\omega T^{\mathrm{e}}_k(\mathbf{x},\mathbf{x}')} = \sum_{\text{even } k=2}^{\infty} (-1)^{k/2} A^{\mathrm{e}}_k(\mathbf{x},\mathbf{x}') e^{i\omega T^{\mathrm{e}}_k(\mathbf{x},\mathbf{x}')}, \qquad (3.19)$$

where $\Omega_R = \Omega_R(\mu_{\mathrm{e}})$ is the real part of the QNM frequency (in the large-L limit) divided by L [32], $A^e_k \equiv \pi\chi_e/\Omega_R(\mu_e)$ and T^e_k is the value of the Boyer-Lindquist time such that $g_e(\mu_e) = -\pi k$. That is, T^e_k corresponds to an approximation of the time at which the null geodesic that starts at x' and passes through k caustics reaches the point x.

The third and last[5] of the contributions to the Green function in Eq. (3.16), G_{BC}, corresponds to the branch cut of the modes $G^{\omega}_{\mathrm{ret}}(\mathbf{x},\mathbf{x}')$ starting at the origin in the complex-frequency plane (e.g., [20,29,30]). This contribution is related to wave scattering by the Coulomb-type potential and it yields the well-known power-law tail decay at late times [20,29,33,34]. This part of the Green function is smooth in the time domain at least after the time when the first, direct null geodesic has joined x and x' [20,23,26,35]. Furthermore, any divergence of G_{BC} before the arrival of the direct null geodesic is purely due to the exponential Fourier factor and so the contribution in the frequency domain from the Fourier transform of G_{BC} is of little-oh order $o(1)$ [26]. As a result, we neglect this piece of the Green function in the high-frequency limit.

[4]After the Fourier transformation, the t dependence of μ_e and χ_e is replaced by the specific value of t such that the corresponding δ-Dirac distribution in Eq. (3.18) becomes singular. Therefore, in the frequency domain they are functions of k, $\mathbf{x}$ and $\mathbf{x}'$.

[5]We note that in Kerr space-time there may be extra branch cuts in the complex-frequency plane due to the spheroidal eigenfunctions and eigenvalue but, in that case, we also expect their Fourier transform to be of order $o(1)$ for large frequency.

IV. EVALUATING THE WAVE PROPAGATION AND POAM

The analysis in the previous section implicitly assumes that the wave emission is coherent within any time interval we are considering, as we have taken the integration lower bound to be "$-\infty$" in Eq. (3.4). This assumption may not be astrophysically realistic, because the typical radio telescope's bandwidth is of the order of GHz, and the time difference between the direct pulse and all the later pulses linearly scales with the black-hole mass M, which is of the order of microseconds if $M \sim M_\odot$ (solar mass). In particular, for supermassive back holes with masses $\geq 10^5 M_\odot$, the coherence time of the wave is much shorter compared to M, in which case the contributions from the δ-Dirac distributions in the G_{QNM} are no longer important. Nevertheless, for the sake of completeness, in the following analysis we shall consider two limiting cases: the coherence length of the wave being much longer or shorter than the black-hole size. We shall find that the POAM spectra that a distant observer receives are completely different in these two scenarios.

A. "Infinite" coherence length

With the coherence length much longer than the black-hole size, the coherent part of the wave that arrives at an observer can be described by the sum of terms in Eqs. (3.9) and (3.19). These terms all contain fast-oscillating phase factors which are proportional to ω, and slowly varying amplitude factors. From now on we will consider the observer to be located far away from the black hole and the source of radiation. The observation plane is orthogonal to the direction of propagation of the wave, i.e., constant-r surface (locally a plane), $r = r_f$. For a fixed emitter location $\mathbf{x}'$, the phase factors T_0 and T^{e}_k are just functions of the observer location $\mathbf{x} = (r_f, \theta_f, \phi_f)$, in Boyer-Lindquist coordinates (r, θ, ϕ). We choose a point with coordinates $\mathbf{x}_0 = (r_f, \theta_0, \phi_0)$ on the observation plane as the origin, and expand the phase functions as

$$T(\mathbf{x}) \approx T(\mathbf{x}_0) + \left.\frac{\partial T}{\partial \theta_f}\right|_{\mathbf{x}_0} \delta\theta_f + \left.\frac{\partial T}{\partial \phi_f}\right|_{\mathbf{x}_0} \delta\phi_f, \qquad (4.1)$$

where $\mathbf{x}$ is a point on the observation plane, $T(\mathbf{x})$ generically denotes T_0 and T^e_k, and from now on we omit

$\mathbf{x}'$ from the argument of $T(\mathbf{x})$ and from that of the amplitudes [it is understood in Eq. (4.1) and similar expressions below that $\mathbf{x}'$ and r_f are fixed].

For later convenience, we further define a new coordinate system on the observation plane to be $(x_1, x_2) \equiv (\delta\theta_f, \sin\theta_0 \delta\phi_f)$ and we define $\zeta \equiv x_1 + ix_2$, with its complex conjugate given by $\zeta^* = x_1 - ix_2$ and its absolute value by $|\zeta| = \sqrt{x_1^2 + x_2^2}$. The latter is related to the cylindrical radial coordinate introduced in Sec. II as $\rho = |\zeta| r_f$. The expansion of the phase in terms of the new coordinates is just

$$T(\mathbf{x}) \approx T(\mathbf{x}_0) + \left.\frac{\partial T}{\partial \theta_f}\right|_{\mathbf{x}_0} x_1 + \left.\frac{\partial T}{\partial \phi_f}\right|_{\mathbf{x}_0} \frac{x_2}{\sin\theta_0} = T(\mathbf{x}_0) + \left.\frac{\partial T}{\partial x_1}\right|_{\mathbf{x}_0} x_1 + \left.\frac{\partial T}{\partial x_2}\right|_{\mathbf{x}_0} x_2. \tag{4.2}$$

As the detector is usually far away from the source, the characteristic values of $x_{1,2}$ or $|\zeta|$ are of the scale of b/r_f where, as introduced earlier, b is the size of the detector. In addition to the "high frequency" assumption $\omega M \gg 1$, we further assume that

$$\eta \equiv \omega M b / r_f \ll 1, \tag{4.3}$$

which is equivalent to saying that the instrument size b is much smaller than the Airy disk size $\lambda r_f / M \sim 2\pi r_f/(\omega M)$ of the diffraction pattern. For a given radiation frequency ω, in order to maximize η, one can either build longer telescope arrays or target the black holes with the largest angular sizes M/r_f in the sky. The best known supermassive black-hole candidates would be the one in the galaxy Messier 87 or Sagittarius A* in our own Galaxy. Take, for example, the millimeter-wavelength sources near Sagittarius A* if the size of the telescope array is comparable to the Earth radius, i.e., $b \sim 6 \times 10^3$ km, the resulting η is about 0.6.

Under the above assumptions, we can expand the phase factors as

$$e^{i\omega T(\mathbf{x})} \approx e^{i\omega T(\mathbf{x}_0)} \left[1 + i\omega \left(\left.\frac{\partial T}{\partial x_1}\right|_{\mathbf{x}_0} x_1 + \left.\frac{\partial T}{\partial x_2}\right|_{\mathbf{x}_0} x_2 \right)\right]. \tag{4.4}$$

It is straightforward to show that Eq. (4.4) only generates $l = \pm 1$ components in the POAM spectrum (it also generates an $l = 0$ component but it has zero orbital angular momentum), because of the linear dependence in $x_{1,2}$. If we included higher order terms in $x_{1,2}$ in the power series expansion in Eq. (4.2), the $|l| \geq 2$ components would also show up in the POAM spectrum, but with weaker spectra weights since $\sqrt{w_l/w_1} \propto \eta^{|l|-1} \ll 1, \ \forall |l| \geq 2$. Therefore, in the following analysis we focus on the $l = \pm 1$ components of the spectrum.

Combining Eqs. (3.9), (3.19), (2.9) and (3.6) and Eq. (4.4) in Eq. (3.6), we obtain the following expression for $\psi_{\omega,\pm 1}$:

$$\psi_{\omega,1} = \frac{iN|\zeta|\omega}{2} A_0(\mathbf{x}_0) e^{i\omega T_0(\mathbf{x}_0)} \left.\frac{\partial T_0}{\partial \zeta}\right|_{\mathbf{x}_0} + \frac{iN|\zeta|\omega}{2} \sum_{\text{even}k=2}^{\infty} (-1)^{k/2} A_k^e(\mathbf{x}_0) e^{i\omega T_k^e(\mathbf{x}_0)} \left.\frac{\partial T_k^e}{\partial \zeta}\right|_{\mathbf{x}_0}, \tag{4.5}$$

$$\psi_{\omega,-1} = \psi_{\omega,1}(\zeta \to \zeta^*), \tag{4.6}$$

where $A_0(\mathbf{x}_0)$ and $A_k^{\mathrm{e}}(\mathbf{x}_0)$ are approximations to $A_0(\mathbf{x})$ and $A_k^e(\mathbf{x})$, respectively (omitting the argument $\mathbf{x}'$). For any real-valued function $T(x_1, x_2) = T(\zeta, \zeta^*)$, we notice that the following relation always holds:

$$\left(\frac{\partial T}{\partial \zeta}\right)^* = \frac{\partial T}{\partial \zeta^*}. \tag{4.7}$$

1. Schwarzschild black hole

In the case that the host black hole is a Schwarzschild black hole, the phase functions T_0 and T_k^{e} are symmetric with respect to the plane spanned by the emitter, the center of the black hole and the receiver. Due to this mirror symmetry, the function $T(\mathbf{x})$ in Eq. (4.2) only depends on one variable, which is the projection of (x_1, x_2) onto the mirror-symmetry plane—see Fig. 2. This one-parameter dependence directly leads to the finding that all the complex numbers $\partial T/\partial\zeta$ in Eq. (4.5) share the same argument in the complex plane, i.e., the ratio between any two of these numbers is real. Combining this fact with Eq. (4.7), it is straightforward to show that $|\psi_{\omega,1}| = |\psi_{\omega,-1}|$, and similarly for the POAM-spectrum weights with $|l| \geq 1$. In other words, Schwarzschild POAM spectra are always symmetric.

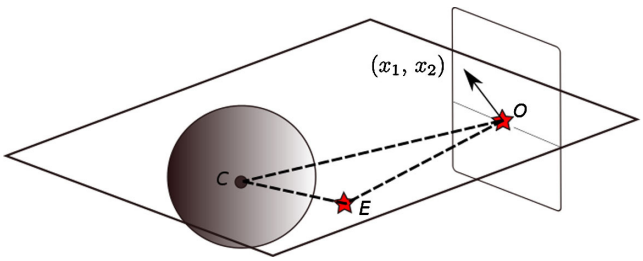

FIG. 2 (color online). An illustration of the relative positions of the emitter E (at $\mathbf{x}'$), the origin of the observation plane O (at $\mathbf{x}_0$) and a Schwarzschild black hole centered at the point C. The arrow points to a point with coordinates (x_1, x_2) on the observation plane. The triangle that contains the points E, O, C lies on the mirror-symmetry plane.

2. Kerr black hole

It is however reasonable to expect asymmetric POAM spectra for radiation sourced near generic Kerr black holes, as originating from the interference between the direct signal and the secondary signals. In the geometrical optics picture, in order to generate nonzero POAM along the optical axis, the propagation directions of these rays must not lie on the same plane[6] (this condition is not satisfied in the case of a Schwarzschild black hole) and the rays with constant phase have to offset each other at the places where a detection is made. The first condition is satisfied if $\partial T_0/\partial\zeta$ and $\partial T^e_k/\partial\zeta$ do not have the same argument in the complex plane, and the second condition is true when $\omega T_0(\mathbf{x}_0)$ and $\omega T^e_k(\mathbf{x}_0)$ are not in phase. It is generic to meet both conditions for emitters near a rotating black hole.

Since, on dimensional grounds, the phase functions T_0 and $T^{\rm e}_k$ are proportional to M, we find that $\psi_{\omega,\pm1} \sim |\zeta|\omega M$ and $\sqrt{w_{\pm1}} \sim \omega M b/r_f = \eta$ for small η. In order to illustrate this asymmetry, we choose the emitter's and receiver's locations to be, respectively, $\mathbf{x}' = (r_i, \theta_i, \phi_i) = (8M, \pi/2, 0)$ and $\mathbf{x} = (r_f, \theta_f, \phi_f) = (10^4 M, 2\pi/3, 0)$, the radiation frequency to be $\omega = 4\pi/M$, and, using the techniques described in Sec. III we calculate $A^{\rm e}_k$, A_0, $\psi_{\omega,\pm1}$ and $w_{\pm1}$. In the top Fig. 3 we plot $\sqrt{w_{\pm1}}/\eta$ with varying black-hole spin a. This plot shows that the spectral asymmetry $|\sqrt{w_1} - \sqrt{w_{-1}}|$ is of the order of $10^{-2}\eta$. In making this plot, we only kept the primary pulse and the secondary pulse with $k = 2$ [note $g_{\rm e}(\mu_{\rm e}) = -\pi k$ does not have a solution for $k = 0$ in this case, and the summation in Eq. (4.5) starts from $k = 2$]. In the bottom of Fig. 3 we plot $A^{\rm e}_{k=2}/A_0$ with varying black-hole spin a. This plot shows that the secondary images can be almost as bright as the primary image: $A^{\rm e}_k/A_0 = O(0.1)$, depending on the emitter's and receiver's locations, as well as the spin of the black hole.

Although it is unnatural to expect the coherence length of the wave to be longer than the size of astrophysical black holes (a coherence length which is comparable to the size of a solar-mass black hole requires the detection bandwidth to be below MHz; for supermassive black holes, such as Sagittarius A*, the corresponding bandwidth is below 0.1 Hz), the primary and secondary signals from the same-time emission are still coherent with each other, and they arrive at Earth at different times. This means that there is nonzero correlation within the time-series data of the field $\langle E(t)E(t+\tau')\rangle$ (where E is the electromagnetic field and we here neglect its polarization), if we set the delay time τ' to be the time lag between the direct signal and other secondary signals [36]. The significance of this correlation should be comparable to $A^{\rm e}_k/A_0$, which could be at least of order $O(0.1)$.

[6]The propagation direction of these rays is not along the r axis, because the phase functions $T(x_1, x_2)$ of these rays are not constant on the celestial sphere.

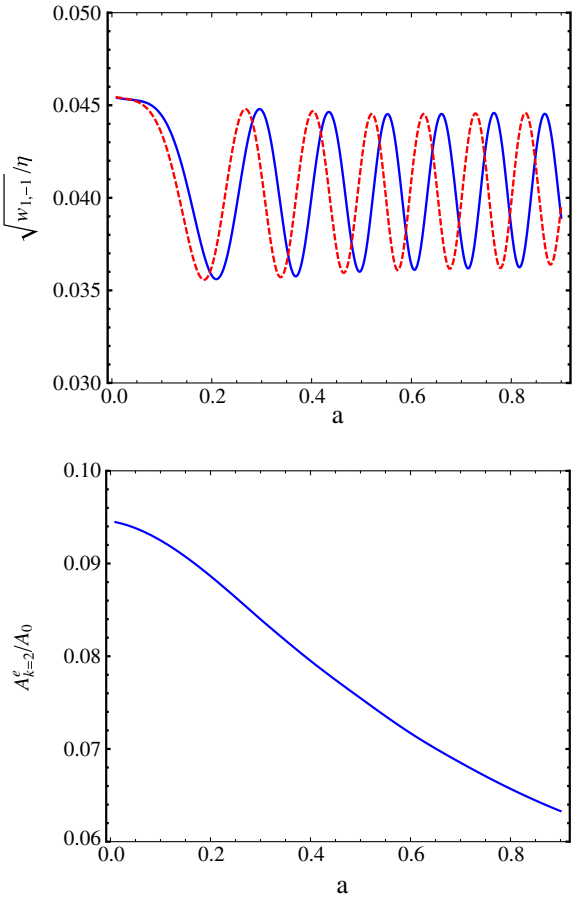

FIG. 3 (color online). Top figure: $\sqrt{w_1}/\eta$ (blue solid line) and $\sqrt{w_{-1}}/\eta$ (red dashed line) for different black-hole spins. The emitter and the receiver are respectively located at $(r_i, \theta_i, \phi_i) = (8M, \pi/2, 0)$ and $(r_f, \theta_f, \phi_f) = (10^4 M, 2\pi/3, 0)$. For illustration purposes, ω is chosen to be $4\pi/M$ to avoid too many oscillations. The spectral asymmetry vanishes for Schwarzschild black hole ($a = 0$), and oscillates as varying black-hole spin, because of the changing phase difference between the primary image and the secondary image $k = 2$. Bottom figure: the ratio between $A^{\rm e}_{k=2}$ and A_0 for the same parameter settings.

B. Incoherent emission

In this subsection, we consider a more realistic scenario where the coherence length of the emission is much shorter than the size of the black hole. In this case, the signal has a contribution from the primary pulse that travels on the light cone and from the coherent follow-ups [which here they correspond to the tail $V(x, x')$, not to the secondary pulses] which lag only a short amount of time (compared to the characteristic time lag between different pulses) after the primary pulse.

Because of the finite-coherence effect, we shall only consider the contribution from the primary pulse and the follow-up signal described by $V(x, x')$. Physically, this is justified by noticing that the part of the follow-up signal which lags far behind the primary signal contributes insignificantly to the total coherent wave. Mathematically, this

may be achieved, for example, by assigning a small imaginary part to the wave frequency, i.e., replacing ω by $\omega + i\epsilon$ with $\epsilon > 0$, and, at the end of the calculation, taking the limit $\epsilon \to 0^+$. As a result of this operation, the coherent wave is evaluated to be

$$\psi_\omega(x) \approx N\left[A_0(\mathbf{x},\mathbf{x}') + \frac{v_0(\mathbf{x},\mathbf{x}')}{i\omega}\right]e^{-i\omega T_0}. \quad (4.8)$$

In order to fully incorporate the finite-coherence effect, the monochromatic emission from the source should be generalized to one with a frequency spectrum. In this case, the wave arriving at the distant observer would be

$$\Psi(x) = \int d\omega f(\omega)\psi_\omega(\mathbf{x})e^{-i\omega t}, \quad (4.9)$$

where $\langle f(\omega)f^*(\omega')\rangle = 1/(2\pi)S_\omega\delta(\omega-\omega')$ ($\langle\rangle$ stands for the ensemble average in random process) and S_ω is the normalized frequency-spectra density of the source: $\int d\omega S_\omega = 1$. In the following analysis, however, we shall stick to the monochromatic approximation in discussing the effect of interference—it is straightforward to include multiple frequencies using Eq. (4.9), and it turns out that the monochromatic case already captures the main physics (about POAM spectrum) here.

The spectra components $\psi_{\omega,0}$ [which plays a part via the overall normalization I in Eq. (2.11)] and $\psi_{\omega,\pm1}$ can be obtained by performing the angular integration described in Eq. (2.9), thus yielding

$$\begin{aligned}\psi_{\omega,0} &\approx N\left[A_0(\mathbf{x}_0) - \frac{v_0}{i\omega}\right]e^{i\omega T_0},\\ \psi_{\omega,+1} &\approx \frac{iN|\zeta|\omega}{2}\left[A_0 - \frac{v_0}{i\omega}\right]e^{i\omega T_0}\frac{\partial T_0}{\partial\zeta}\bigg|_{\mathbf{x}_0}\\ &\quad + \frac{N|\zeta|}{2}e^{i\omega T_0}\frac{\partial A_0}{\partial\zeta}\bigg|_{\mathbf{x}_0}, \end{aligned} \quad (4.10)$$

$$\psi_{\omega,-1} \approx \psi_{\omega,1}(\zeta \to \zeta^*). \quad (4.11)$$

The above expressions show that in the large-frequency limit these tail effects are subdominant to those from the direct wavefront. That is, $\psi_{\omega,\pm1}$ are still dominated in the high-frequency limit by the direct pulse that travels on the light cone, with a magnitude of order $|\zeta|\omega M$. However, the term with $\partial T_0/\partial\zeta$ in Eq. (4.10) and the corresponding term in Eq. (4.11) contribute evenly to the magnitude of $\psi_{\omega,\pm1}$ or $w_{\pm1}$. Therefore, the POAM spectral asymmetry arises from the beating between the amplitude and phase variations of the direct signal, the latter variation being suppressed by a $1/(\omega M)$ factor. In other words, although the spectrum weight is still $\sqrt{w_{\pm1}} \sim \eta$, the spectral asymmetry scales as $|\sqrt{w_1} - \sqrt{w_{-1}}| \sim b/r_f$ for small η. In fact, this net POAM is expected to originate from the frame-dragging effect of rotating black holes, and it vanishes in a Schwarzschild background. As suggested by Eq. (4.10), if the amplitude modulation does not follow the same direction as the phase modulation on the celestial sphere, these "unbalanced" rays will generate a nonzero contribution to the angular momentum along the r axis. From another point of view, the black-hole rotation breaks the mirror symmetry in detection that we discussed for Schwarzschild black holes, and the beating of phase and amplitude modulations introduces a net POAM, even though it is extremely small.

For millimeter-wavelength sources near Sagittarius A*, even if the size of the telescope array is of the scale of the Earth radius 6×10^3 km, the spectral asymmetry b/r_f is of the order of 10^{-14} which is way too weak to be measured. On the other hand, the pure spectrum weights $\sqrt{w_{\pm1}} \sim \eta$ are of the order of 0.6. Therefore, it seems feasible that these $l \neq 0$ spectrum components could be resolved by coherent detection by spatially separated telescopes. However, as we recall from the discussion in Sec. II, the symmetric part of the POAM spectrum is degenerate with the tilt angle of the observation plane. In order to extract information about the black hole from the POAM measurement, it might be necessary to use the asymmetric part of the spectrum, which is extremely small in this case.

We note that the result we have obtained in this subsection of weak POAM-spectrum asymmetry is different from that obtained in [8]. The reason is that, as mentioned, the physical settings are different, since in [8] they consider an extended source, as opposed to our pointlike source, while they assume the emission from the whole accretion disk around a black hole to be spatially coherent. Thus, their main asymmetry effect comes from the interference between the radiation from different parts of the disk, as opposed to it being due to the light-twisting effect that we have studied in this subsection (or to interference between different rays emitted from the same point and arriving at different times as we saw in the previous subsection).

V. RECEIVERS NEAR AN OPTICAL CAUSTIC

The analysis in Sec. IV is invalid if the receiver is located close to an optical caustic (defined below). At such a point, the Hadamard form Eq. (3.7) for the Green function and the high-oscillation-frequency asymptotics of Eq. (3.17) for the QNM contribution to the Green function both fail. As we shall show below, the wave intensity is amplified near an optical caustic, which increases the detectability of the source. While for a pointlike source[7] near a black hole we expect the chance of Earth being located near an optical caustic point of its radiation to be small, we expect the chances to be significantly higher if the source is *extended*. It still remains physically interesting to understand the

[7]It could be star, or a flare with extraordinary brightness in the accretion disk.

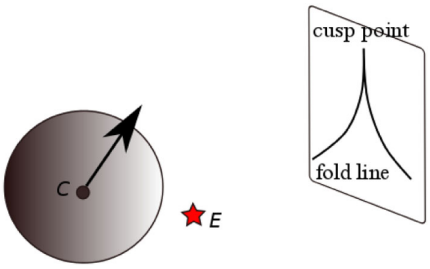

FIG. 4 (color online). An illustration of potential optical caustic structure on the celestial sphere/observation plane, due to an emission source *EE* near a spinning black hole centered at *C*. *Fold* lines meet each other at a *cusp* point.

wave near an optical caustic and to exploit the corresponding POAM spectrum.

In the following analysis, we shall heavily apply the techniques and results of *catastrophe optics*, which is expounded in the excellent text by Berry and Upstill [37]. Interested readers can also find detailed numerical investigations of the optical caustic structure in Kerr space-time in [38], and its relation with x-ray variability in [39]. We now briefly introduce the main concepts and terminology.

At a given distance, the receiver's sky location can be characterized by the two-parameter family (θ_f, ϕ_f) or (x_1, x_2), which are often referred to as *control parameters* in catastrophe optics and which we denote by C_i, $\forall i$. In its turn, the angles of the emitted rays are usually referred to as *state variables* and we denote them generically by s_j, $\forall j$. The "action function" $T_0(\mathbf{x}, \mathbf{x}')$ [see Eq. (3.9)], when viewed as a function of the null rays (for fixed $\mathbf{x}$ and $\mathbf{x}'$) is generally a multivalued function. It can be made into a single-valued function by including a functionality on the state variables (which allow us to uniquely characterize a null ray). Such single-valued function is called a "generating function" and we denote it by $\Phi(s_j; C_i)$. Null rays are those paths that extremize the generating function, i.e., such that $\partial\Phi/\partial s_j = 0$, $\forall j$. Optical caustics, then, correspond to *singularities* of this gradient map. A *structurally stable singularity* is a singularity of the above gradient map such that if it is perturbed, it is related to the new singularity by a diffeomorphism of C_i. For example, the singularities or optical caustics in Schwarzschild space-time are structurally unstable, as they are susceptible to small perturbations of the space-time. However, a *fold* line or a *cusp* point (described below and illustrated in Fig. 4) in Kerr space-time are generically stable singularities. As explained in [37], all the structurally stable singularities can be classified into different equivalence classes called *catastrophes*, with a generating function associated to each class.

A. Cusp point

It turns out that the only catastrophe with a two-dimensional control-parameter space has the following generating function:

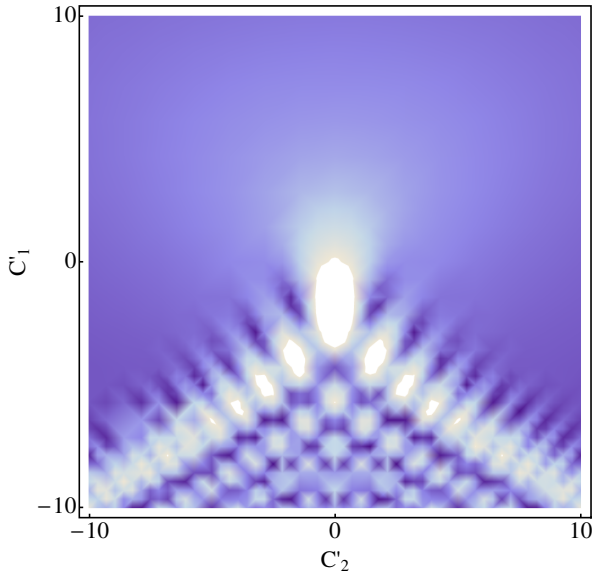

FIG. 5 (color online). A contour plot of the integral in Eq. (5.4) (which is proportional to the wave function near a cusp point), where a darker region corresponds to a region with a higher wave amplitude and where the axis corresponds to generic rescaled control parameters $C'_{1,2}$.

$$\Phi(s; C_1, C_2) = \frac{s^4}{4} + \frac{s^2}{2}C_2 + sC_1, \tag{5.1}$$

where s refers to the state variable that matters for the singularity classes (the other state variable does not affect the singularity class) and $C_{1,2}$ are the control variables. In the case we are considering, $C_{1,2}$ can be mapped to $x_{1,2}$ under proper rotation and rescaling (here, $C_{1,2}$ and $x_{1,2}$ are all dimensionless, so the rescaling factors should also be dimensionless). The singularity point at $C_{1,2} = 0$ is usually called a "cusp" in catastrophe theory. It is also worth noting that one can always add any additional independent state variable s', with associated generating functions that are at most quadratic (for example s'^2), and it does not affect the singularity structure. With this generating function, the wave function[8] near a cusp is approximately

$$\psi_\omega(C_1, C_2) \propto \sqrt{\omega}\int_{-\infty}^{\infty} ds e^{i\omega\Phi(s;C_1,C_2)}. \tag{5.2}$$

The proportionality factor in Eq. (5.2) is independent of ω; we will not write out such proportionality factor throughout this section. See Fig. 5 for an illustration of the wave function near a cusp point. In order to extract the frequency dependence of ψ_ω, we make a transformation of the variables s and $C_{1,2}$:

[8]Strictly speaking, ψ_ω in Eq. (5.2) should be referred to as the spatial part of the wave function, but given the simple relation Eq. (3.6), in this section we will loosely refer to it as the wave function itself.

$$s' \equiv \omega^{1/4} s, \qquad C_1' \equiv \omega^{3/4} C_1, \qquad C_2' \equiv \omega^{1/2} C_2. \quad (5.3)$$

Then ψ_ω becomes

$$\psi_\omega(C_1, C_2) \propto \omega^{1/4} \int_{-\infty}^{\infty} ds' e^{i\Phi(s'; C_1', C_2')}, \quad (5.4)$$

which implies that the amplitude of the wave is amplified by a $(\omega M)^{1/4}$ factor near a cusp. For millimeter-wavelength sources near a supermassive black hole with mass comparable to Sagittarius A*, this is an order of 10^7 amplification in the intensity.

We can also determine the POAM spectrum from Eq. (5.2) or Eq. (5.4). Let us denote by (C_1^0, C_2^0) the control variables corresponding to the location of the origin of the telescope array. We then expand the control variables as $C_1 = C_1^0 + \delta C_1, C_2 = C_2^0 + \delta C_2$. Correspondingly, the wave function on the observation plane can be expanded as

$$\psi_\omega \propto \omega^{1/4} \int_{-\infty}^{\infty} ds' \left(1 + i \frac{\partial \Phi}{\partial C_1'} \delta C_1' + i \frac{\partial \Phi}{\partial C_2'} \delta C_2'\right) e^{i\Phi_0}, \quad (5.5)$$

where we have defined $\Phi_0 \equiv \Phi(s'; C_1'^0, C_2'^0)$.

Performing the POAM decomposition with respect to the above wave function, we find that the main contribution comes from the term with $\delta C_1'$ in Eq. (5.5), which gives $\sqrt{w_{\pm 1}} \sim (\omega M)^{3/4} b/r_f$. The interference between the terms with $\delta C_2'$ and with $\delta C_1'$ generates the asymmetry in the POAM spectrum, which is $|\sqrt{w_1} - \sqrt{w_{-1}}| \sim (\omega M)^{1/2} b/r_f$. For a millimeter-wavelength source near Sagittarius A*, if Earth happens to be close to a cusp point in the celestial sphere, the inferred POAM spectral asymmetry is about 10^{-7}, which is still too weak to be measured.

B. Fold line

There is another possibility, perhaps with a higher chance than a cusp, which is that Earth is located close to the singularity described by a *fold* line. This happens when only one of the two coordinates on the celestial sphere is the "control variable," and the phase is linear in the other variable. According to catastrophe theory, there is only one catastrophe that has a one-dimensional control space, and its characteristic polynomial is given by

$$\Phi(s; C_1) = \frac{s^3}{3} + sC_1, \quad (5.6)$$

with the line associated with $C_1 = 0$ usually referred to as a "fold" line. Let us denote the coordinate along the fold line as C_2 (for a specific value of C_2 we have a fold point, and as the value of C_2 varies continuously we have a fold line) and the generating function along the fold line as $\Theta(C_2)$. Then the wave function near a fold line is

$$\begin{aligned}\psi_\omega(C_1, C_2) &\propto \sqrt{\omega} \int_{-\infty}^{\infty} ds e^{i\omega[\Phi(s;C_1)+\Theta(C_2)]} \\ &= \omega^{1/6} \int_{-\infty}^{\infty} ds' e^{i[\Phi(s';C_1')+\omega\Theta(C_2)]} \\ &= 2\pi\omega^{1/6} \mathrm{Ai}(C_1') e^{i\omega\Theta(C_2)}, \end{aligned} \quad (5.7)$$

where $\mathrm{Ai}(x)$ denotes the Airy function which is real valued—see Fig. 6 for an illustration. The new variables s' and C_1' are here defined as

$$s' \equiv \omega^{1/3} s, \qquad C_1' \equiv \omega^{2/3} C_1. \quad (5.8)$$

We can see from Eq. (5.7) that the wave intensity is amplified by a factor of $(\omega M)^{1/3}$ near a fold line, which is brighter than a generic point on the celestial sphere, but dimmer than a cusp point. Similar to the analysis performed near a cusp point, we expand the celestial coordinates in the observation plane as $C_1 = C_1^0 + \delta C_1, C_2 = C_2^0 + \delta C_2$, and the wave function can also be expanded as

$$\begin{aligned}\psi_\omega(C_1, C_2) - \psi_\omega(C_1^0, C_2^0) \propto 2\pi\times \\ \omega^{1/6} \left[\frac{\partial \mathrm{Ai}(C_1')}{\partial C_1'} \delta C_1' + i \frac{\partial \Theta}{\partial C_2} \delta C_2 \mathrm{Ai}(C_1')\right] e^{i\omega\Theta}. \end{aligned} \quad (5.9)$$

Correspondingly, we obtain the strength of $\sqrt{w_{\pm 1}}$ to be proportional to η, which comes from the phase variation along the fold line; the asymmetry $|\sqrt{w_1} - \sqrt{w_{-1}}|$ is directly proportional to $(\omega M)^{2/3} b/r_f$ and it is attributed to the phase beating between Φ and Θ. For a millimeter-wavelength source near Sagittarius A*, if Earth happens to be close to the fold line in the celestial sphere, the inferred POAM spectral asymmetry is about 10^{-5}.

As we have already seen from the wave behavior near a fold line or a cusp point, the generating functions are not proportional to ω along the control variables's direction,

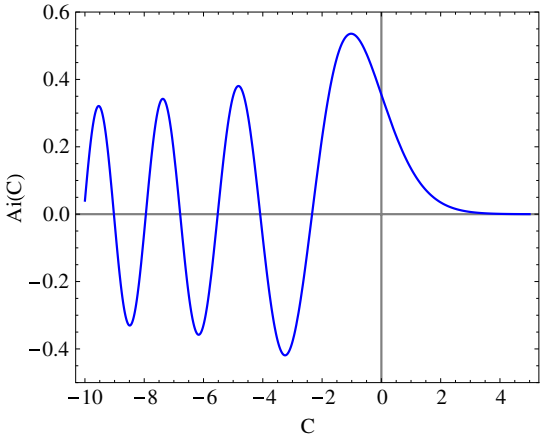

FIG. 6 (color online). Plot of the Airy function, which describes the wave function dependence on a control variable C near a fold point via Eq. (5.7).

and the amplitudes usually oscillate fast. This happens because a family of light rays merges with each other at the optical caustic, and their interference gives these unusual frequency dependences. It is the same merging interference which also generates the net POAM shown here.

VI. CONCLUSION

In this work, we have studied a wave that is emitted near a rotating black hole and eventually reaches a distant observer. We demonstrated that measuring the distortion of the wavefront provides an independent channel for obtaining information about the source, in addition to light bending or other spectroscopic measurements. In order to characterize the wavefront distortion, we have adopted the previously established POAM decomposition and we have applied it to the wave, which we have computed using the retarded Green function in Kerr space-time. While the POAM spectra of waves scattered by Schwarzschild black holes are shown to be always symmetric, any rotation in the host black hole generically generates asymmetry in the POAM spectrum. Since the symmetric part of the spectrum is degenerate with the tilt angle of the observation plane, we have concluded that it is more likely to extract information about the source from the asymmetric part.

The resulting POAM spectrum strongly depends on the temporal coherence of the emission source and the sky location of the receiver. On the one hand, we found that the main contribution to the symmetric spectrum weight comes from the phase variation in the sky of the direct signal. For generic receiver locations, the magnitude of the square root of the weight $\sqrt{w_{\pm 1}}$ is of order of η, which is roughly the ratio between the size of the telescope and the Airy disk size of the image, and it could be as large as 0.6 for millimeter-wavelength sources near Sagittarius A*. If the receiver is located near a cusp point on the sky, we have shown, using techniques developed in catastrophe optics, that $\sqrt{w_{\pm 1}} \sim \eta/(\omega M)^{1/4}$; if the receiver is near a fold line in the sky, we have shown that $\sqrt{w_{\pm 1}} \sim \eta$ instead.

On the other hand, we have shown that the asymmetric part of the POAM spectrum could be generated by the beating between phase and amplitude variation of the primary signal, or by the beating between the phase variation of the primary and secondary signals. This beating reflects the physical origin of nonzero POAM, either by coherently combining rays misaligned optical axis, or by the interference of adjacent light bundles. Nevertheless, we find that the spectral asymmetry is generally too weak to be measured. This is in part due to the large distances between Earth and astrophysical black holes, which serve as strong-gravity lenses or "phase plates." The best candidate for detection might be an extended region in the accretion disk near Sagittarius A* such that Earth lies near a fold line of its radiation. In this case, the spectral asymmetry for the $|l| = 1$ mode can be as large as 10^{-5}. However, even with advanced techniques available to cancel the effects from atmosphere turbulence, e.g., adaptive optics methods, this signal is still far below the sensitivity of current radio telescopes, such as millimeter-wavelength very long baseline interferometry arrays.

ACKNOWLEDGMENTS

We thank Barry Wardell, Latham Boyle, Avery Broderick and Haixing Miao for many helpful discussions. H. Y. thanks Yanbei Chen for introducing this project and providing valuable comments on the manuscript. This research is funded by NSF Grants No. PHY-1068881 and No. PHY-1005655, CAREER Grants No. PHY-0956189 and No. PHY-1055103, NASA Grant No. NNX09AF97G, the Sherman Fairchild Foundation, the Brinson Foundation, and the David and Barbara Groce Startup Fund at Caltech. H. Y. acknowledges supports from the Perimeter Institute for Theoretical Physics and the Institute for Quantum Computing. M. C. thanks the Perimeter Institute for Theoretical Physics for hospitality and financial support. Research at Perimeter Institute is supported by the Government of Canada and by the Province of Ontario though the Ministry of Research and Innovation.

[1] C. Tamm and C. O. Weiss, J. Opt. Soc. Am. B **7**, 1034 (1990).
[2] A. Mair, A. Vaziri, G. Weihs, and A. Zeilinger, Nature (London) **412**, 313 (2001).
[3] J. Leach, M. J. Padgett, S. M. Barnett, S. Franke-Arnold, and J. S. Courtial, Phys. Rev. Lett. **88**, 257901 (2002).
[4] G. Molina-Terriza, J. P. Torres, and L. Torner, Phys. Rev. Lett. **88**, 013601 (2001).
[5] G. Gibson, J. Courtial, M. Padgett, M. Vasnetsov, V. Pasko, S. Barnett, and S. F. Arnold, Opt. Express **12**, 5448 (2004).
[6] J. Y. Vinet, Phys. Rev. D **82**, 042003 (2010).
[7] M. Harwitt, Astrophys. J. **597**, 1266 (2003).
[8] F. Tamburini, B. Thide, G. M. Terriza, and G. Anzolin, Nat. Phys. **7**, 195 (2011).
[9] E. Poisson, A. Pound, and I. Vega, Living Rev. Relativity **14**, 7 (2011).
[10] H. Yang, F. Zhang, A. Zimmerman, and Y. Chen, Phys. Rev. D **89**, 064014 (2014).
[11] N. M. Elias II, Astron. Astrophys. **492**, 883 (2008).

[12] K. S. Thorne and R. D. Blandford, *Modern Classical Physics: Optics, Fluids, Plasmas, Elasticity, Relativity, and Statistical Physics* (Princeton University Press, Princeton, NJ, 2014).
[13] A. E. Siegman, *Lasers* (University Science Books, Sausalito, CA, 1986), Chap. 16.
[14] B. Thide, H. Then, J. Sjoholm, K. Palmer, J. Bergman, T. D. Carozzi, Ya. N. Istomin, N. H. Ibragimov, and R. Khamitova, Phys. Rev. Lett. **99**, 087701 (2007).
[15] A. E. E. Rogers, S. S. Doeleman, and J. M. Moran, Astron. J. **109**, 1391 (1995).
[16] A. Broderick (private communication).
[17] A. C. Ottewill and B. Wardell, Phys. Rev. D **84**, 104039 (2011).
[18] M. Casals, S. Dolan, A. C. Ottewill, and B. Wardell, Phys. Rev. D **79**, 124044 (2009).
[19] S. R. Dolan and A. C. Ottewill, Phys. Rev. D **84**, 104002 (2011).
[20] M. Casals and A. Ottewill, Phys. Rev. Lett. **109**, 111101 (2012).
[21] A. Zenginoglu and C. R. Galley, Phys. Rev. D **86**, 064030 (2012).
[22] M. Casals, S. Dolan, A. C. Ottewill, and B. Wardell, Phys. Rev. D **79**, 124043 (2009).
[23] M. Casals, S. Dolan, A. C. Ottewill, and B. Wardell, Phys. Rev. D **88**, 044022 (2013).
[24] B. Wardell, C. R. Galley, A. Zenginoglu, M. Casals, S. R. Dolan, and A. C. Ottewill, Phys. Rev. D **89**, 084021 (2014).
[25] F. G. Friedlander, *The Wave Equation on a Curved Space-Time* (Cambridge University Press, Cambridge, England, 1975).
[26] M. Casals and A. Ottewill, Phys. Rev. D **86**, 024021 (2012).
[27] C. W. Misner, K. S. Thorne, and J. A. Wheeler, *Gravitation* (W. H. Freeman and Co., San Francisco, 1973).
[28] M. Casals and B. C. Nolan, Phys. Rev. D **86**, 024038 (2012).
[29] E. W. Leaver, Phys. Rev. D **34**, 384 (1986).
[30] E. S. C. Ching, P. T. Leung, W. M. Suen, and K. Young, Phys. Rev. D **52**, 2118 (1995).
[31] B. Mashhoon, Phys. Rev. D **31**, 290 (1985).
[32] H. Yang, D. A. Nichols, F. Zhang, A. Zimmerman, Z. Zhang, and Y. Chen, Phys. Rev. D **86**, 104006 (2012).
[33] R. H. Price, Phys. Rev. D **5**, 2419 (1972).
[34] S. Hod, Phys. Rev. Lett. **84**, 10 (2000).
[35] M. Casals and A. Ottewill, Phys. Rev. D **87**, 064010 (2013).
[36] L. Boyle and M. Russo, arXiv:1110.2789.
[37] M. V. Berry and C. Upstill, in *Progress in Optics*, edited by E. Wolf (Elsevier, New York, 1980), Vol. 18.
[38] V. Bozza, Phys. Rev. D **78**, 063014 (2008).
[39] K. Rauch and R. Blanford, Astrophys. J. **421**, 46 (1994).